The Journal of Engineering

IET International Radar Conference (IRC 2018)

IET Journals
The Institution of Engineering and Technology

Deflection characterisation of rotary systems using ground-based radar

eISSN 2051-3305
Received on 21st February 2019
Accepted on 7th May 2019
E-First on 28th August 2019
doi: 10.1049/joe.2019.0503
www.ietdl.org

Francis X. Ochieng[1], Haoyang Jiang[2], Craig M. Hancock[1] ✉, Gethin W. Roberts[3], Julien Le Kernec[2,4], Xu Tang[1], Huib de Ligt[1]

[1]*Department of Civil Engineering, University of Nottingham – Ningbo China, Zhejiang, People's Republic of China*
[2]*University of Electronic, Science and Technology of China, Chengdu, People's Republic of China*
[3]*The University of the Faroe Islands, Faroe Islands*
[4]*The University of Glasgow, UK*
✉ *E-mail: craig.hancock@nottingham.edu.cn*

Abstract: In the last two decades, an increase in large rotary machines/systems has been witnessed. To ensure safe operation of these systems especially due to extreme stress caused by centrifugal forces as well as the wind or water loadings, regular structural health monitoring (SHM) of the unbalanced parameters, particularly at the blade tips is necessary. For this, the use of non-contact sensors provides the most appropriate approach; however, millimetric out-of-plane deflection monitoring using non-contact sensors at distances >1 m has not been comprehensively addressed for rotary systems, like wind turbines. This study presents a modelling environment to simulate radar returns to analyse rotary systems. Employing Sammon mapping as a dimensionality reduction procedure in conjunction with 2D visualisation, the study demonstrates the characterisation of dynamic deflection parameters using a fast, portable ground-based interferometric radar (GBR). Comparisons between the GBR results with those of a Leica AR20 GPS indicate a divergence ±12.79 mm. The study utilises SHM framework to acquire, normalise, extract, and validate GBR signals within an SHM framework for structures under test or for deflection validation of the new system. Further, it contributes to the non-contact structural fatigue damage detection during design, testing, and operating stages of rotary structures blade tips.

1 Introduction

During the design of mega-cantilevered rotating structures such as long wind-turbine blades, accurate prediction of the time-varying transient wind loads generated due to the unsteady environmental and operating conditions is essential to enable correct estimation of fatigue life of structures and detect and prevent damage. In particular, this is important for large wind turbine blades and their design is determined by the fatigue rather than ultimate load [1].

In determining optimal dynamic behaviour, structural integrity, and stability aspects of a cantilevered-like structure exposed to aerodynamic and structural loadings, the structure's dynamic modal characterisation [deflection and modal parameters (mode shapes and natural frequencies)] is of critical importance [2, 3].

Studies on structural health monitoring (SHM) of rotating cantilevered-like structures using non-contact sensors have, to the best of our knowledge, been limited. This is despite the significant benefits non-contact SHM sensors could offer in monitoring rotating cantilevered-like structures. Non-contact SHM sensors for blade tip deflection take one of the three forms: electromagnetic [4], laser-based [5, 6], and radio waves [7].

The non-contact monitoring of blade deflection allows changes affecting blade structure or operational integrity to be identified by variations in the deflection envelop. For instance, loosening of a blade bolt, mass change due to accretion of ice, excessive blade vibration, and geometric changes arising from impact with an external object will affect the deflection. However, previous works reveal a challenge in non-contact out-of-plane deflection monitoring at great distances.

The goal of this study is first to utilise the GBR as a vibration-based sensor to acquire dynamic out-of-plane deflection characterisation of cantilevered-like physical model of a rotating blade and validate the results within a SHM framework. Second, it demonstrates GBR as a SHM non-contact sensor is able to undertake vibration-based damage detection (VBDD) [3, 8, 9] of structures that due to technical difficulty, costs, and inappropriateness in use of contact sensors [9, 10] have had limited field and laboratory tests undertaken on them [11–13].

The study in Section 2 presents the modelling environment and preliminary results obtained with it compared to established methods. Section 3 then introduces the working theory of GBR, which forms the basis of using it in the experimental set-up detailed in Section 4. The results and discussion of how GBR integrates in SHM framework are discussed Section 5 and a conclusion made in Section 6.

2 Experimental framework

A simulation and practical framework are employed in this study. The practical framework is based on a cantilevered arm that is rotating on a horizontal axis, with an out-of-plane deflection in the vertical axis (Fig. 1). The rotating cantilevered arm models an actual wind turbine with rotors rotating in the vertical axis and the out of plane deflection along the horizontal. This wind turbine models form the simulation framework. Hence allows two synergetic experimental frameworks to be utilised in this study.

For the simulative framework, a large wind turbine was modelled in Matlab using canonical shapes to simulate the radar cross-section of the different parts of the blades and mast (Fig. 2). The radar was placed at 1 m above ground and slightly displaced from the rotation plane to get a reasonable projection of Doppler in the radial direction. Although the best position would be at 90°, the wind turbine nacelle rotates so we took an example angle that was not ideal on purpose. In our simulation, the wind turbine first accelerates in rotation reaches maximum rotational speed and then stopped.

The transmitted signal used in this model was a chirp from 4 to 4.5 GHz with 0.02 μs pulse width. The pulse repetition frequency was set at 500 Hz; this gives an unambiguous velocity of ±7.14 m/s or 25.7 km/h. It is of course insufficient for large wind turbines but we started with slow rotations to validate our concept change first. Future work will focus on getting simulation results including

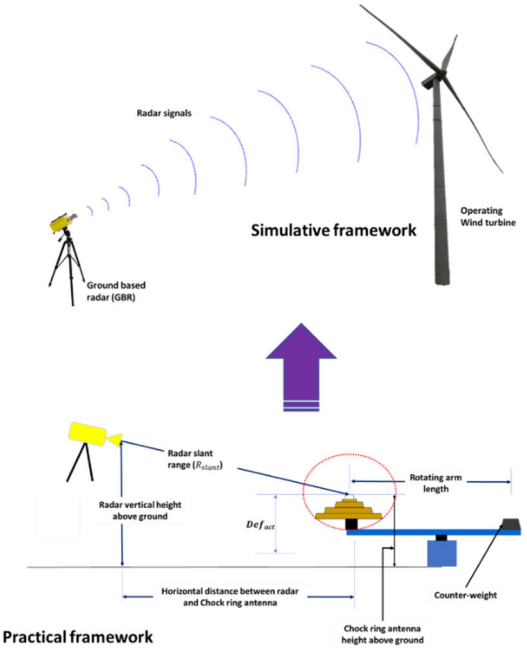

Fig. 1 *Linking framework of rotating arm to wind turbine*

deformation matching the experimental radar parameter from 17.1 to 17.3 GHz at a bandwidth of 165 MHz. The radar pulse will be adapted as well for unambiguous measurements.

Two types of processing methods were applied to the data generated by the two frameworks: a time-deflection analysis method building on the Sammon mapping [14] to compare the deflections from the practical framework. For the simulative framework, a time-frequency analysis method generating a two-dimensional time-frequency spectrum [15] and a range-Doppler analysis method generating three-dimensional information including time-frequency-range declined into two approaches: Chen's approach [15] and our proposed method.

2.1 Sammon mapping

The basis for deflection characterisation is the VBDD. This normally employs contact and now non-contact sensors to acquire mainly typical unbalanced parameters [16, 17]. Such parameters include radial displacement, modal frequency, modal damping, and modal shape [11, 18–21]. The parameters can be acquired from multiple sensors or from the outputs of a single sensors, as part of the 3 tier SHM framework.

The three-tier framework consists of three tiers or steps. As a first step, the data is normalised and binned, then as a second step, either a time-deflection or time-frequency visualisation is developed, from which extraction of features (condition/unbalanced parameters) is done. Finally, based on the analysis of the features, a decision is made on the health of the structure.

For feature extraction using GBR for discontinuous deflection monitoring (that is one of short time duration), a Sammon map matrix ($M_{\text{sammon\_map}}$) is developed by analysing the time-deflection 2D visualisations. This is achieved by the extension of the method given in [14] to provide a $2 \times N$ Sammon mapping matrix with the deflection (Def_{act}) on second column and time (T) or Fourier amplitude spectrum on the first as shown in (1)

$$M_{\text{sammon\_map}} = \begin{bmatrix} T_1 & \text{Def}_{\text{act1}} \\ T_2 & \text{Def}_{\text{act2}} \\ \vdots & \vdots \\ \vdots & \vdots \\ \vdots & \vdots \\ T_n & \text{Def}_{\text{actn}} \end{bmatrix} \quad (1)$$

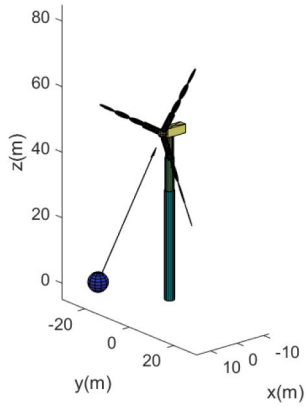

Fig. 2 *Wind turbine model for radar simulations*

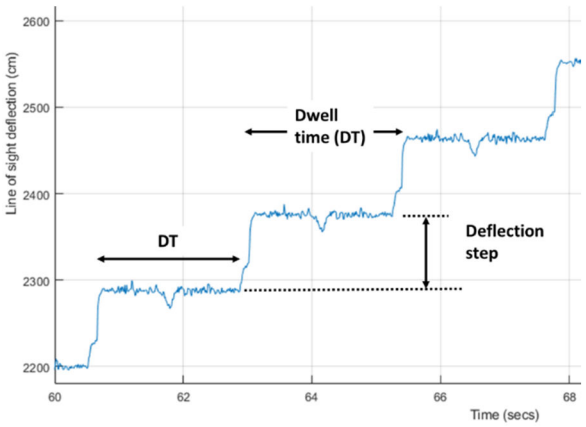

Fig. 3 *GBR deflection spectrum*

This is, however, based on two hypothesis: (i) the data is cyclical (Fig. 3), as would be the case for a rotary system, and (ii) the dwell time for each cyclical data slot is tractable i.e. <360 s.

2.2 Chen's method

One of the challenges of radar simulation is that the signal frequency is usually high, and according to the Shannon–Nyquist theorem, the sampling frequency should be at least twice the maximum frequency. In this case, the size of the sampled data will be large and the computational load will increase dramatically as the radar carrier frequency increases. Chen's method considers the radial space with a set range and a set resolution, each point target reflector is assigned to a range bin from which a set delay is calculated. This leads to a phase difference in the received signal as shown in (2).

$$s_r(t) = \mathrm{e}^{j2\pi \mathrm{F}(t-\tau)} \quad (2)$$

$$\tau \simeq \frac{2R_0(t)}{c} \quad (3)$$

where $R_0(t)$ is the time-dependent distance between the target and the radar, F is the carrier frequency, c is the speed of light. Generating the time-domain signal and received signals from all the point targets is relatively cumbersome and, therefore, it can be simplified as shown in (4).

$$s_1(t) = \frac{s_r(t)}{s(t)} = \frac{\mathrm{e}^{j2\pi \mathrm{F}(t-\tau)}}{\mathrm{e}^{j2\pi \mathrm{Ft}}} = \mathrm{e}^{-j2\pi \mathrm{F}\tau} = \mathrm{e}^{-j2\pi \mathrm{F}(2R_0(t)/c)} \quad (4)$$

where $s(t)$ is the transmitted signal, $s_1(t)$ sums up this Doppler information only and the signal can be sampled at the pulse repetition frequency of choice and saves computational load. The modelling method is described in Algorithm 1 (see Fig. 4).

```
01. Define radar parameters
02. Initialize physical model
03. Set PRF, carrier frequency, resolution
04. Defined simulation model parameters
05. Set speed, dimensions, car model
06. returnedsignal = 0;
07. for m=1:numberOfEllipsoidsInModel
08.         Calculate radar return for m^th ellipsoid
09.         returnedSignal = returnedSignal+m^th radar return;
10. end for
11. Spectrogram generation
12. Apply STFT method on returnedSignal
```

Fig. 4 *Algorithm 1*

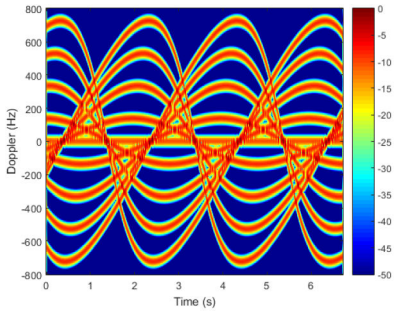

Fig. 5 *Wind turbine spectrogram with Chen's method*

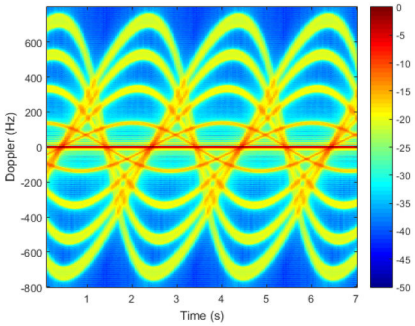

Fig. 6 *Wind turbine spectrogram obtained with our method*

2.3 Our method

Chen's method executes rapidly but it does not allow to get any information such as range maps and range-Doppler images which offer a lot of information that can be used for further analysis. In order to explain the algorithm, the transmitted signal (which can be set arbitrarily) used in this experiment is defined in (5) for a chirp.

$$s(t) = \Re\left(\text{Rect}\left(T - \frac{T}{2}\right)e^{j2\pi(F + (B/T)t)t}\right) \tag{5}$$

where T is the pulse duration (20 ns), B the bandwidth, F the starting frequency and the pulse repetition period is 2 ms. The sampling frequency is set to 10 GHz. The received signal is defined in (6) and illustrated in Figs. 5 and 6 for every reflector defined and associated with the radar cross-section σ.

$$s_r(t) = \sigma s(t - \tau) \tag{6}$$

The algorithm is described in pseudo-code in Algorithm 2 (see Fig. 7). It can be observed that our method, although slower than Chen's method, gives greater details in simulation of spectrograms as shown in Figs. 2 and 5 especially in acceleration and deceleration phases. Furthermore, it also gives access to raw radar returns, range maps, range-Doppler images which enable multimodal analysis which is not possible with Chen's method. This will be used to optimise the radar placement and configuration for the extraction of unbalanced parameters as the signal,

```
01. Initialization of Radar parameters
02. Initialize physical model
03. Signal definition
04. Define time scales
05.         shortTime – 0 to max return time at Fs
06.         longTime=0 to max animation time at PRF
% generate raw return signal;
07. for n = 1 to max animation time
08.         Initialize returnSignal
09.         for m = 1: numberOfReflectorsInModel
10.                 Calculate distance/delay of m^th reflector
12.                 Calculate RCS of the m^th reflector
13.                 Calculate signal return of m^th reflector;
14.                 returnSignal = returnSignal+ pulse;
15.         end for
16. end for
% generate range-Doppler images
17. Set number of pulses per frame, overlap
18. Calculate the number of frames (range-Doppler images)
19. Match filtering on every received signal
20. for i = 1 to number of frames
21.         Calculate Range-Doppler image (i)
22.         Spectrogram(i) = incoherent sum in range(Range-Doppler image(i))
23. end for
```

Fig. 7 *Algorithm 2*

frequency is configurable. The wind-turbine model will be exploited for deflection characterisation after further development and will be considered for future publications.

3 Methodology

3.1 Ground-based radar (GBR) system

The GBR for this experiment is a coherent IBIS-S™ quasi-monostatic radar system, with two collocated antennae – one for transmitting and other for receiving. The system was operated at Ku band at a median frequency of 17.2 GHz, instantaneous bandwidth of 200 MHz, and a frequency step increment of between 30 and 300 kHz, with a dwell time duration of 3.3 to 33 µs and radiated power (EIRP) of 26 dBm [22]. A maximum acquisition frequency of 200 Hz is utilised.

3.2 GNSS/GPS system

A Leica AR25 antenna and a Leica Viva GS 10 receiver were utilised to capture the vertical deflection [23]. The Leica AR25 four constellation GNSS choke ring antenna is a 3D antenna using a new ultra-wideband Dorne–Margolin element [23] for high accuracy and performance due to multi-path rejection and improved low elevation tracking. Hence, it can be placed at ground level as shown in Fig. 8. The system had a deflection accuracy of ±2 cm when connected in RTK/DGPS mode [23]. In the absence of such connection, the error will increase significantly.

For acquisition and saving of the data, a Leica Viva GS10 receiver is used. The receiver is connected to the antenna and initialised using a GPS 10 rover. The accuracy of the receiver is for a single baseline in real-time kinematic is 8 mm in the horizontal and 15 mm in the vertical. During post-processing, this reduces to 3 and 3.5 mm for the horizontal and vertical, respectively.

3.3 Dynamic deflection characterisation methodology

The GBR was placed on a balcony (Fig. 8), with its height above ground ($\boldsymbol{R_h}$) was 6.7 m, distance between it and choke ring antenna ($\boldsymbol{D}_{\text{cR}}$) 9.72 m, and the radar slant distance being (R_{slant}) being 11.83 m. The height between the ground the antenna ($\boldsymbol{A_h}$) was 0.97 m (Fig. 9).

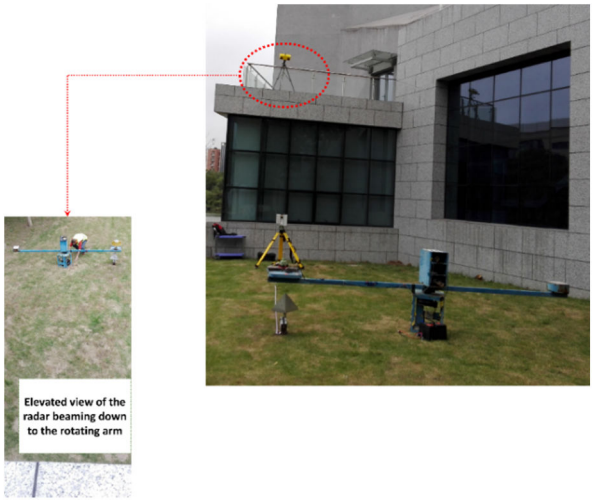

Fig. 8 *GBR view of rotating arm experimental setup*

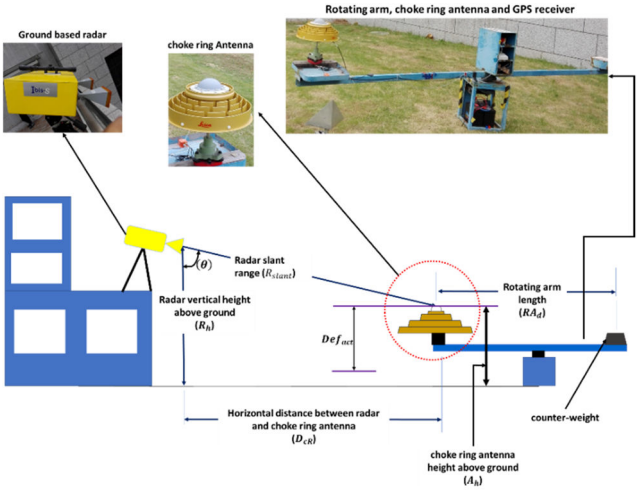

Fig. 9 *Deflection characterisation of a rotary system*

With an effective length **(RA$_d$)** of 4 m, the rotating arm was set to rotate at two different revolutions; a low revolution of 12 rpm and a high one of 36 rpm. This simulated the different rotations a wind turbine undergoes at low and at high wind speeds.

3.4 Experimental set-up

The GBR provides a deflection only if the target is moving along the line of sight (LoS). Thus, for vertical motion (flexural or flap wise motion) of the rotating arm tip where the choke ring antenna is placed; the GBR must be pointed directly above the structure (Fig. 9). For rotational movements, which then involve lateral movements, the GBR is placed at an angle to the direction of motion of the structure.

The actual movement along the LoS (DefLoS) [24, 25] is thus provided by (7). The GBR determines the displacements by comparing the phase delay ($\Delta\phi$) of the emitted and reflected radio waves (8)

$$\mathrm{Def}_{\mathrm{LoS}} = \frac{1}{4}\frac{\lambda}{(\pi)}(\Delta\phi) \tag{7}$$

$$\mathrm{Def}_{\mathrm{act}} = \frac{R_o(\mathrm{Def}_{\mathrm{LoS}})}{R_{\mathrm{slant}}} = \mathrm{Def}_{\mathrm{LoS}} \times \cos(\theta) \tag{8}$$

where R_o is the distance between the radar position and the target, R_{slant} is the slant range and θ is the declination angle i.e. angle at which the GBR is inclined to face the choke ring antenna. In [25], a SNR above 60 dB is recommended for distances below 1 km. In the event that the radar is placed at an angle to the structure as was the case here, $\mathrm{Def}_{\mathrm{act}}$ is then provided by (9) [25].

$$\mathrm{Def}_{\mathrm{act}} = \frac{\mathrm{Def}_{\mathrm{LoS}}}{\cos[(\pi/2) - (\alpha_b - \theta)]} \tag{9}$$

where α_b and α_{gbr} are the slope angles of the beam and the GBR, respectively. Equation (9) assumes the GBR is pointed orthogonally at the choke antenna and θ is the declination angle of the GBR antenna from the horizontal (Fig. 9).

Subsequently, based on this characteristics and analysis of both experimental and simulated data, it was determined the closest range one can use the GBR to determine the out-of-plane deflection of a rotary systems. To do this, a four-step procedure was followed.

(a) The GBR and GPS were started and took measurements, with the rotating arm at stationary position. The aim of the static test was to enable the GPS to obtain the exact height of the choke ring antenna, above ground level

(b) After the static test, the arm remote switch was pressed to start the motor and subsequently the arm started to rotate. Measurements from both GBR and GPS were taken at this constant low speed revolutions (12 rpm).

(c) The revolution speed was then increased to 36 rpm, leading to higher vertical deflections of the rotating arm. This simulated an increase wind speeds impacting a wind turbine blade

(d) Finally, the rotating arm was stopped.

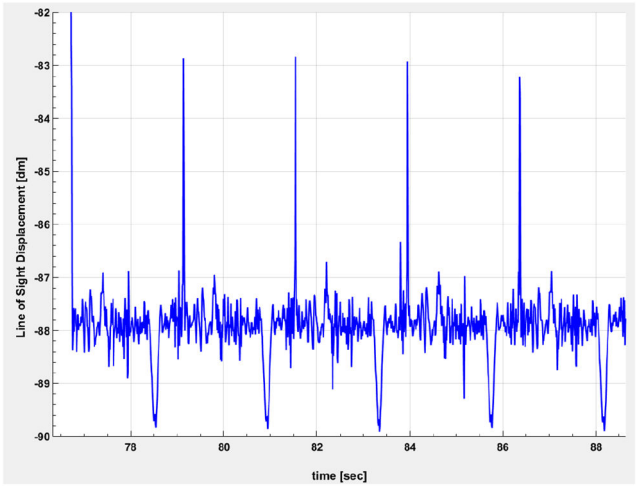

Fig. 10 *Excerpt of GBR deflection for choke ring antenna*

4 Results and discussion

4.1 Feature extraction using Sammon method

The deflection of the choke antenna was captured by the GBR and GPS/GNSS. Fig. 10 demonstrates the deflection obtained in decimetres from the excerpt of 110 s of scan number 3. The major troughs/dips approximating about 2.3 decimetres (dm) represent the deflection, while the slender peaks approximating about 5 dm. The distance between each major dip is 2.4 dm.

Between the peaks and troughs are the flashes which are echoes obtained as the choke rings rotates from its orthogonal position through the almost parallel position (may explain the slender peaks) to wave propagation direction of GBR signals and round back to the orthogonal position.

The excerpt obtained in Fig. 10 is part of the deflection in Fig. 3. In Fig. 3, each dwell time lasts about 2.2 s, in which one deflection dip is observed. Afterwards, a deflection jumps of about 9.1 dm occurs before the next dwell time. The GBR determines two kinds of out of plane deflections – the deflections as the choke ring antenna moved towards the ground (vertical down) and when it moved up away from the ground level (vertical up) (Fig. 10).

When considered closely, it is demonstrated that the vertical down and vertical up deflections (Fig. 3) have similar patterns and dwell times though at different steps/jumps (Fig. 3). This provides

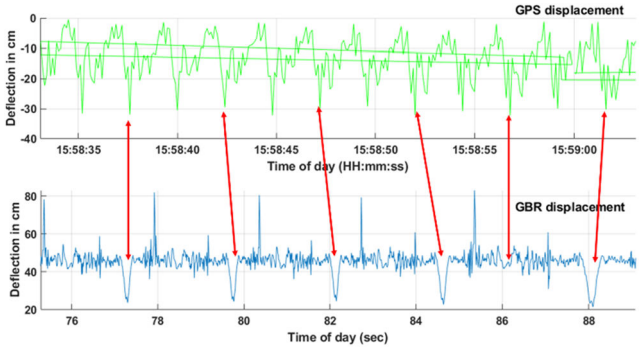

Fig. 11 *Sammon map visualisation of sensors*

Table 1 Average deflection between GBR and GNSS/GPS

Sensor type	Mean deflection, cm	Error bands, cm
GBR	23.38	23.3796 ± 0.01
GNSS/GPS	24.111	24.111 ± 3

the first criteria in utilising the Sammon mapping when extending visually, the repetitiveness. From Fig. 3, a time-based excerpt of GBR and GPS signals can be visually checked over a shorter span out of the whole measurement to provide a 2D visualisation of the Sammon map matrix. (Fig. 11).

Despite a slight shift in time, it can be observed that when the GBR deflection occurs, those are the same places the GPS also obtains maximum deflections. This may be attributed to the GBR bandwidth and GPS sampling frequency. The GBR utilises a bandwidth of 165 Hz, thus in every revolution of 2.75 s, a deflection is registered. The GPS acquisition is 20 Hz, hence for one revolution, three deflections will be registered (0.33333 for each deflection), with the third deflections coinciding with the GBR deflection. However, due to slight difference in timings and the frequencies, a shift is seen.

4.2 Validation of GBR as non-contact sensor

Table 1 shows the results of comparing the average deflections between the two sensors.

The analysis of average deflection between the GBR and GNSS/GPS shows a deviation of ±3.12%. This proves that the GBR can be used for non-contact deflection monitoring sensor within the three-tier SHM framework. The study was limited, however, in that it did not consider other unbalanced parameters such as modal frequency, which is key in SHM monitoring of cantilevered-like structures. Future works will consider incorporating the modal frequencies in the GBR monitoring, as well as using an actual wind turbine once we validate a proof-of-concept first.

5 Conclusion

The work has demonstrated that even from 11.87 m in slant range, the GBR provides data almost as accurate as the GPS for the out-of-plane deflection. The work has demonstrated that under the assumptions of periodicity and tractability of total data acquisition time, Sammon mapping can be utilised to extract results by considering short excerpts/extracts of the repetitive time-deflection visualisation to extract and assess the SHM features within the three-tier framework.

6 Acknowledgments

The authors acknowledge the financial support from the International Doctoral Innovation Centre, Ningbo Education Bureau, Ningbo Science and Technology Bureau, and the University of Nottingham. This work was also supported by the Ningbo Science and Technology Bureau as part of the International Academy for the Marine Economy and Technology (IAMET) project 'Structural Health Monitoring of Infrastructure in the Logistics Cycle (2014A35008)'

7 References

[1] Liu, X., Lu, C., Liang, S., *et al.*: 'Vibration-induced aerodynamic loads on large horizontal axis wind turbine blades', *Appl. Energy*, 2017, **185**, pp. 1109–1119

[2] Larsen, G.C., Hansen, M.H., Baumgart, A., *et al.*: '*Modal analysis of wind turbine blades*' (2002), ISBN:87-550-2696-6

[3] Nguyen, T.-C., Huynh, T.-C., Kim, J.-T.: 'Numerical evaluation for vibration-based damage detection in wind turbine tower structure', *Wind Struct.*, 2015, **21**, (6), pp. 657–675

[4] Procházka, P.: 'Sensors for noncontact vibration diagnostics in rotating machinery'. AIP Conf. Proc., Ancona, Italy, 2016, **1740**, (1), p. 020002

[5] Giri, P., Lee, J.R.: 'In situ blade deflection monitoring of a wind turbine using a wireless laser displacement sensor device within the tower'. Key Engineering Materials, Durnten-Zurich, Switzerland, 2013, 558, pp. 84–91

[6] Gwashavanhu, B., Oberholster, A.J., Heyns, P.S.: 'Rotating blade vibration analysis using photogrammetry and tracking laser Doppler vibrometry', *Mech. Syst. Signal Process*, 2016, **76**, pp. 174–186

[7] Woike, M., Abdul-Aziz, A., Clem, M.: 'Structural health monitoring on turbine engines using microwave blade tip clearance sensors'. Smart Sensor Phenomena, Technology, Networks, and Systems Integration, San Diego, CA, USA, 2014, 9062, p. 90620L

[8] Siebel, T., Friedman, A., Koch, M., *et al.*: 'Assessment of mode shape-based damage detection methods under real operational conditions'. 6th European Workshop on Structural Health Monitoring, Dresden, Germany, 2012

[9] Kim, W., Yi, J.-H., Kim, J.-T., *et al.*: 'Vibration-based structural health assessment of a wind turbine tower using a wind turbine model', *Procedia Eng.*, 2017, **188**, pp. 333–339

[10] Larsen, G.C., Berring, P., Tcherniak, D., *et al.*: 'Effect of a damage to modal parameters of a wind turbine blade'. EWSHM-7th European Workshop on Structural Health Monitoring, Nantes, France, 2014

[11] Wymore, M.L., Van Dam, J.E., Ceylan, H., *et al.*: 'A survey of health monitoring systems for wind turbines', *Renew. Sust. Energy Rev.*, 2015, **52**, pp. 976–990

[12] Liu, W.Y., Tang, B.P., Han, J.G., *et al.*: 'The structure healthy condition monitoring and fault diagnosis methods in wind turbines: a review', *Renew. Sust. Energy Rev.*, 2015, **44**, pp. 466–472

[13] Schubel, P.J., Crossley, R.J., Boateng, E.K.G., *et al.*: 'Review of structural health and cure monitoring techniques for large wind turbine blades', *Renew. Energy*, 2013, **51**, pp. 113–123

[14] Loh, C.-H., Hsueh, W., Tu, Y.-C., *et al.*: 'Vibration-based damage assessment of structures using signal decomposition and two-dimensional visualization techniques', *Struct. Health Monit.*, 2018, **18**, pp. 991–1009, doi:10.1177/1475921718765915

[15] Chen, V.C.: '*The micro-Doppler effect in radar*' (Artech House, Norwood, MA, USA, 2011)

[16] Mao, W., Liu, G., Li, J., *et al.*: 'An identification method for the unbalance parameters of a rotor-bearing system', *Shock Vib.*, 2016, **2016**, p. 9

[17] Gong, X., Qiao, W.: 'Simulation investigation of wind turbine imbalance faults'. Int. Conf. on Power System Technology, Hangzhou, People's Republic of China, 2010

[18] Cooperman, A., Martinez, M.: 'Load monitoring for active control of wind turbines', *Renew. Sust. Energy Rev.*, 2015, **41**, pp. 189–201

[19] Beganovic, N., Söffker, D.: 'Structural health management utilization for lifetime prognosis and advanced control strategy deployment of wind turbines: an overview and outlook concerning actual methods, tools, and obtained results', *Renew. Sust. Energy Rev.*, 2016, **64**, pp. 68–83

[20] Ruan, J., Ho, S.C.M., Patil, D., *et al.*: 'Structural health monitoring of wind turbine blade using piezoceremic based active sensing and impedance sensing'. 2014 IEEE 11th Int. Conf. on Networking, Sensing and Control (ICNSC), Miami, FL, USA, 2014, pp. 661–666

[21] Kasera, A.A., Ochieng, F.X., Kinyua, R.: 'Design and testing of an efficient savonius wind turbine's rotor blade for low wind speed applications', *J. Sustain. Res. Eng.*, 2015, **2**, (1), pp. 23–35

[22] IDS, IBIS-L system User manual Italy: 'Ingegmeria dei sistemi SpA (IDS)', 2010, p. 65

[23] AG, L.G.: '*LEica Viva GNSS GS10 – data sheet*', in AG, L. G. (Ed.): (Leica Geosystems AG, Heerbrugg, Switzerland, 2015), p. 2

[24] Ozdemir, C.: '*Inverse synthetic aperture radar imaging with MATLAB algorithms*' (Wiley, Portland, USA, 2012)

[25] Gentile, C., Bernardini, G.: 'Radar-based measurement of deflections on bridges and large structures', *Eur. J. Environ. Civil Eng.*, 2010, **14**, (4), pp. 495–516